

MULTI-RELAXATION-TIME LATTICE BOLTZMAN MODEL FOR UNIFORM-SHEAR FLOW OVER A ROTATING CIRCULAR CYLINDER

by

Hasan NEMATI, Mousa FARHADI*, Kurosh SEDIGHI, and Ehsan FATTAHI

Faculty of Mechanical Engineering, Babol University of Technology, Babol, Islamic Republic of Iran

Original scientific paper

UDC: 536.24:532.527:517.938

DOI: 10.2298/TSCI100827082N

A numerical investigation of the two-dimensional laminar flow and heat transfer a rotating circular cylinder with uniform planar shear, where the free-stream velocity varies linearly across the cylinder using multi-relaxation-time lattice Boltzmann method is conducted. The effects of variation of Reynolds number, rotational speed ratio at shear rate 0.1, blockage ratio 0.1, and Prandtl number 0.71 are studied. The Reynolds number changing from 50 to 160 for three rotational speed ratios of 0, 0.5, and 1 is investigated. Results show that flow and heat transfer depends significantly on the rotational speed ratio as well as the Reynolds number. The effect of Reynolds number on the vortex-shedding frequency and period-surface Nusselt numbers is overall very strong compared with rotational speed ratio. Flow and heat conditions characteristics such as lift and drag coefficients, Strouhal number, and Nusselt numbers are studied.

Keyword: *lattice Boltzmann method, multi-relaxation-time, rotating circular cylinders, shear flow, shear rate, laminar flow*

Introduction

Fluid flow and heat transfer around rotating cylinders is a typical process in industry. Furthermore periodic vortex shedding patterns and fluctuating velocity fields behind the bluff bodies can cause structural damage which shortens the life of the structure and increases the acoustic noise and the drag. This structure can be applied in the chemical process, textile industries, transmission cables, making metal plate, and glass and plastics industries. The uniform flow past a circular cylinder has been widely investigated both experimentally and numerically in the past due to the practical and theoretical importance of the flow [1-7]. However, in practice many structures, such as off-shore pipelines near the seabed, are immersed in a boundary layer. These are typical cases with non-uniform approach flows. Therefore, it is important to understand the features of the vortex shedding and hydrodynamic forces of a circular cylinder subject to a non-uniform flow. Some experimental [8-12] and numerical studies have been devoted to linear shear flow around a circular cylinder. However, due to the difficulty of generating shear flow, these studies were restricted to cases with large shear parameters but low Reynolds numbers, or at subcritical Reynolds

*Corresponding author; e-mail: mfarhadi@nit.ac.ir

numbers but with small shears parameters. There have been fewer numerical studies than experimental studies, and the numerical studies were restricted to two-dimensional simulations, with low Reynolds number flows [13, 14]. The most relevant feature of the flow, at moderate values of the Reynolds number, *e. g.* at a Reynolds number (based on the external velocity and cylinder diameter) close to 50, is the instability of the symmetric wake and the onset of a time-periodic regime characterized by alternate vortex shedding, known as the von Karman vortex street, whose dimensionless period depends on the Reynolds number. Sohankar *et al.* [15] have investigated that by further increasing the Reynolds number a transition to three-dimensional flow occurs around the value of 180. However the periodic vortex shedding phenomenon remains the large-scale dominant feature even at large Reynolds number in the turbulent wake. In this study the free-stream with a linear velocity profile fig. 1, $U = U_c + Gy$ and constant temperature T_∞ , passes over a rotating circular cylinder with a diameter D , angular velocity ω and constant temperature T_h .

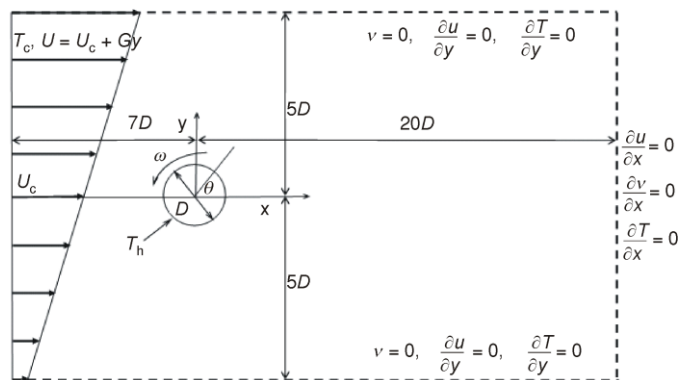


Figure 1. Computational domain and co-ordinate system

Therefore three non-dimensional parameters of flow are important and investigated: one is Reynolds number, twice is rotational speed ratio β , and last non-dimensional parameter is velocity gradient or shear rate K . As we said quite a few studies have been performed on uniform-shear flow over a circular cylinder particularly rotating circular cylinder. They have mainly investigated the effects of Reynolds

number and shear rate on the vortex-shedding frequency, the magnitude and direction of the mean lift, the magnitude of the mean drag, and so on in the uniform-shear flow. Despite many achievements to date, some controversial issues have to be further resolved for improved understanding of the bluff-body flow. Part of the early studies is summarized by Jordan *et al.* [16]. The numerical studies carried out by Jordan *et al.* indicated that the front stagnation point shifted to the high velocity side in the shear flow. However, they reported different results in regard to the direction of the transverse lift force. They found that the average lift was toward the low velocity side of the free-stream, while Tamura *et al.* [13] reported that it was in the opposite direction. The numerical results of Tamura *et al.* showed that the mean drag coefficient increased with the shear parameter, while the experimental results by Kwon *et al.* [11] revealed that the drag coefficient decreased monotonically as the shear parameter increased. One of the useful numerical methods that have been used in the recent years is the lattice Boltzmann method (LBM). It was used for simulating the flow field in wide ranges of the engineering applications such as heat transfer problems [17, 18], phase change problems [19-21], cylindrical structure [22, 23], turbulent flow [24, 25], porous media [26], multiphase flow [27], microchannel [28], *etc.* In the present study, the ability of LBM for simulation the laminar flow and heat transfer a rotating circular cylinder with uniform planar shear, where the free-stream velocity varies linearly across the cylinder, was investigated. The effects of variation of Reynolds number, rotational speed ratio (β) and shear rate (K) at blockage ratio

0.1 and $Pr = 0.71$ are studied. The range of Reynolds numbers of $50 \leq Re \leq 160$ for three rotational speed ratios of 0, 0.5, and 1 and $K = 0.1$ are investigated. The results presented in the form of streamlines, vorticity, and temperature contours and flow characteristics such as lift and drag coefficients, Strouhal number, and Nusselt numbers.

The lattice Boltzmann method

Lattice Boltzmann equation of momentum

In the field of computational fluid dynamics (CFD), two major approaches to simulate fluids have been developed in the last decades. The classical approach is based on the numerical solutions of the Navier-Stokes equations (NS). Equation (1) shows the momentum equation, which ensures the momentum conservation, while eq. (2) shows the continuity equation, which secures the mass conservation. These partial differential equations (PDE) are solved by the discretization of space and time by using finite differences, finite elements, or finite volumes to derive the macroscopic values of pressure p or the fluid velocity \mathbf{u} .

$$\frac{\partial \mathbf{u}}{\partial t} + \mathbf{u} \nabla \mathbf{u} = -\frac{1}{\rho} \nabla p + \frac{1}{\rho} \nabla (\mu \nabla \mathbf{u}) + \mathbf{g}_y \quad (1)$$

$$\frac{\partial \rho}{\partial t} + \nabla (\rho \mathbf{u}) = 0 \quad (2)$$

In contrast to the NS approach, the LBM divides time and space in steps to form a lattice and discretize the fluid as particles, which are positioned at certain points in space, called lattice sites or cells. These fluid particles are only allowed to move in certain and fixed directions, which are derived by a discretization of velocity space [29]. In the LBM, the particle is represented by distribution function. This distribution function is calculated by solving the lattice Boltzmann equation (without external force), eq. (3), which is a special discretization of the kinetic Boltzmann equation. The macroscopic quantities of the simulated fluid can then be derived by calculating the hydrodynamic moments of the distribution function. In contrast to the second-order PDE in the NS approach, the LBM uses only first order PDE:

$$\frac{\partial f}{\partial t} + c \nabla f = -\frac{1}{\tau} (f - f^{\text{eq}}) \quad (3)$$

where c is the particle velocity vector, f^{eq} – the equilibrium distribution function, and τ – the relaxation time due to collision [30] and depending on the fluid viscosity. By a discretization in velocity space, a finite set of velocity vectors is derived, which have to conserve mass, momentum, and energy of the fluid particles (conservation laws). Equation (4) shows the discretized formulation of eq. (3). f_α denotes the corresponding distribution function in direction α , which is associated with the discrete velocity c_α in direction α and f_α^{eq} is the corresponding equilibrium distribution function [30]:

$$\frac{\partial f_\alpha}{\partial t} + c_\alpha \nabla f_\alpha = -\frac{1}{\tau} (f_\alpha - f_\alpha^{\text{eq}}) \quad (4)$$

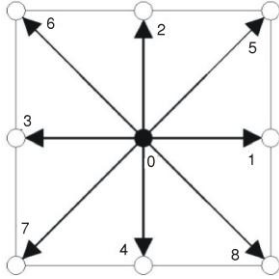


Figure 2. Discrete velocity vectors for the D2Q9 model for 2-D LBM

In this work the velocity space discretization in the two dimensional case is the D2Q9 model [30]. In this model, the velocity space is discretized in 9 distribution functions, which is the most popular model for the 2-D case. Figure 2 shows the 9 velocities of the D2Q9 model. In the following, \mathbf{e}_α will denote the discrete velocity set, where α is between 0 and 8:

$$\mathbf{e}_\alpha = \begin{cases} (0,0) & \alpha = 0 \\ \left\{ \cos\left[(\alpha-1)\frac{\pi}{4}\right], \sin\left[(\alpha-1)\frac{\pi}{4}\right] \right\} c & \alpha = 1, 2, 3, 4 \\ \sqrt{2} \left\{ \cos\left[(\alpha-1)\frac{\pi}{4}\right], \sin\left[(\alpha-1)\frac{\pi}{4}\right] \right\} c & \alpha = 5, 6, 7, 8 \end{cases} \quad (5)$$

where $c = \Delta x / \Delta t$, Δx and Δt are the lattice cell and the lattice time step sizes, respectively.

For simplicity in lattice Boltzmann method assumes $\Delta x = \Delta t = 1$. For the D2Q9 model, the equilibrium distribution function of eq. (4) is expressed as:

$$f_\alpha^{eq} = w_\alpha \left[1 + \frac{3}{c^2} \mathbf{e}_\alpha \mathbf{u} + \frac{9}{2c^4} (\mathbf{e}_\alpha \mathbf{u})^2 - \frac{3}{2c^2} \mathbf{u} \mathbf{u} \right] \quad (6)$$

where

$$w_\alpha = \begin{cases} \frac{4}{9} & \alpha = 0 \\ \frac{1}{9} & \alpha = 1, 2, 3, 4 \\ \frac{1}{36} & \alpha = 5, 6, 7, 8 \end{cases} \quad (7)$$

where w_α is the equilibrium distribution weight for direction α . The fluid density ρ can be evaluated with eq. (8), whereas the velocity \mathbf{u} is contained in the momentum fluxes of eq. (9):

$$\rho = \sum_\alpha f_\alpha \quad (8)$$

$$\rho \mathbf{u} = \sum_\alpha \mathbf{e}_\alpha f_\alpha \quad (9)$$

Equation (4) is called the discrete velocity model (DVM). This equation can be solved by the standard numerical approaches, for example finite difference method. The LBM approach uses this method for discretization of eq. (4):

$$f_\alpha(\mathbf{x} + \mathbf{e}_\alpha \Delta t, t + \Delta t) - f_\alpha(\mathbf{x}, t) = -\frac{\Delta t}{\tau_m} \left[f_\alpha(\mathbf{x}, t) - f_\alpha^{eq}(\mathbf{x}, t) \right] \quad (10)$$

where Δt is the lattice time step, $\Delta x = e_\alpha \Delta t$ – the lattice space step, t_m – the lattice relaxation time, and $\mathbf{x} = xi + yj$ – the a point in the discretized physical space that x , and y are variables from $(0, n)$, and $(0, m)$ respectively. Equations (1) and (2) can be derived for the D2Q9 model as (without force body):

$$\frac{\partial \mathbf{u}}{\partial t} + \mathbf{u} \nabla \mathbf{u} = -\frac{1}{\rho} \nabla p + \nu \nabla^2 \mathbf{u} \quad (11)$$

$$\nabla \mathbf{u} = 0 \quad (12)$$

The pressure p satisfies the equation of state as $p = \rho c_s^2$ and the kinematical viscosity ν is determined by $\nu = c_s^2 (t_m - 0.5)$, where $c_s = c^{1/3}$ – the speed of sound.

Lattice Boltzmann equation of temperature

Lattice Boltzmann equation of temperature field like velocity field can be considered as:

$$g_\alpha(\mathbf{x} + e_\alpha \Delta t, t + \Delta t) - g_\alpha(\mathbf{x}, t) = -\frac{\Delta t}{\tau_h} [g_\alpha(\mathbf{x}, t) - g_\alpha^{\text{eq}}(\mathbf{x}, t)] \quad (13)$$

g_α is the temperature distribution function in the α direction and τ_h – the relaxation time. g_α^{eq} is the corresponding equilibrium distribution function that can be expressed as [31, 32]:

$$g_\alpha^{\text{eq}} = w_\alpha T \left(1 + \frac{3}{c^2} \mathbf{e}_\alpha \cdot \mathbf{u} \right) \quad (14)$$

where T is the fluid temperature and can be evaluated from:

$$T = \sum_\alpha g_\alpha \quad (15)$$

In addition, similar to mass and momentum equations, equation of temperature can be obtained as [30]:

$$\frac{\partial T}{\partial t} + \nabla(\mathbf{u}T) = \sigma \nabla^2 T \quad (16)$$

where σ is the diffusivity coefficient which is represented as $\sigma = c_s^2 (\tau_h - 0.5)$.

Finally, eq. (10) and (13) is usually solved in two steps:

$$\tilde{f}_\alpha(\mathbf{x}, t + \Delta t) = f_\alpha(\mathbf{x}, t) - \frac{1}{\tau_m} [f_\alpha(\mathbf{x}, t) - f_\alpha^{\text{eq}}(\mathbf{x}, t)] \quad \text{Collision step} \quad (17a)$$

$$\tilde{g}_\alpha(\mathbf{x}, t + \Delta t) = g_\alpha(\mathbf{x}, t) - \frac{1}{\tau_h} [g_\alpha(\mathbf{x}, t) - g_\alpha^{\text{eq}}(\mathbf{x}, t)] \quad (17b)$$

$$f_\alpha(\mathbf{x} + e_\alpha \Delta t, t + \Delta t) = \tilde{f}_\alpha(\mathbf{x}, t + \Delta t) \quad \text{Streaming step} \quad (18a)$$

$$g_\alpha(\mathbf{x} + e_\alpha \Delta t, t + \Delta t) = \tilde{g}_\alpha(\mathbf{x}, t + \Delta t) \quad (18b)$$

where \tilde{f}_α , and \tilde{g}_α denotes the post-collision distribution function. Equation (17) is the so called collision step. At first step, various fluid particle interactions are modeled like collisions and calculated new distribution functions according to the distribution functions of the last time step and the equilibrium distribution functions, which are calculated with eq. (6)

and eq. (14). The second step is called the stream step. In this step, fluid particles are streamed from one cell to a neighboring cell according to the velocity and temperature of the fluid particles in this cell. This streaming operation can either be performed as a pushing operation from one cell to the surrounding cells or as pulling operation in one cell from the surrounding cells.

Curved boundary treatment

Consider fig. 3(a) is a part of optional curved wall geometry, where the black circles on the boundary \mathbf{x}_w , the open circles are the boundary nodes in the fluid \mathbf{x}_f and the grey circles show solid area \mathbf{x}_b . To complete the lattice Boltzmann solution, the $\tilde{f}(\mathbf{x}_b, t)$ and $\tilde{g}(\mathbf{x}_b, t)$ in boundaries, are needed. Δ is defined to evaluate the fraction of crossed link in the fluid area:

$$\Delta = \frac{\|\mathbf{x}_f - \mathbf{x}_w\|}{\|\mathbf{x}_f - \mathbf{x}_b\|} \quad (19)$$

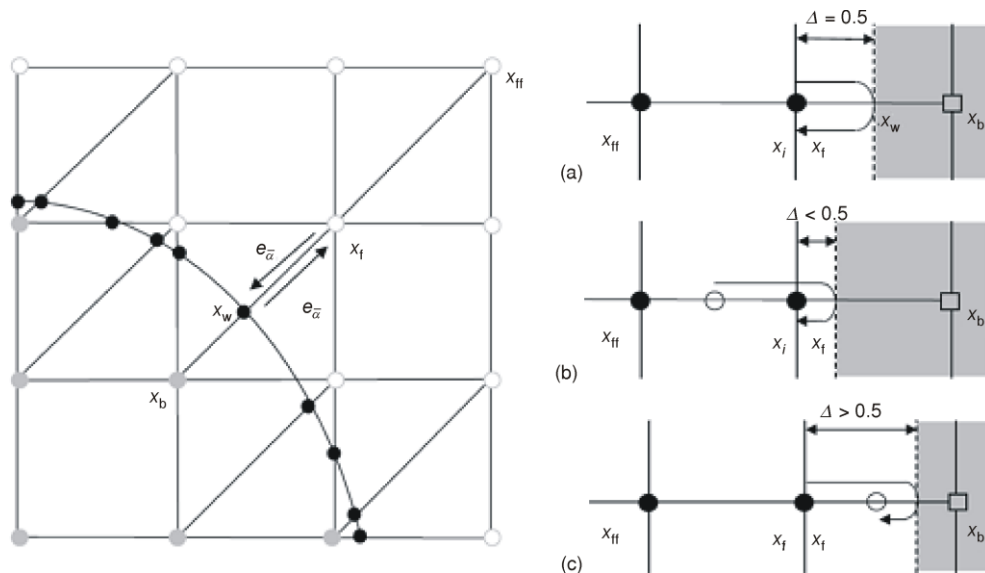


Figure 3. Figure of lattices in curved wall boundary and bounce back; (a) $\Delta = 0.5$, (b) $\Delta < 0.5$, and (c) $\Delta > 0.5$

The standard (half-way) bounce back no-slip boundary condition always assumes a delta value of 0.5 to the boundary wall, fig. 3(b). Due to the curved boundaries, delta values in the interval of (0, 1) are now possible. Figure 3(c) shows the bounce back behavior of a surface with a delta value smaller than 0.5 and fig. 3(d) shows the bounce back behavior of a wall with delta bigger than 0.5. In all three cases, the reflected distribution function $\tilde{f}_{\bar{\alpha}}(\mathbf{x}, t + \Delta t)$ at \mathbf{x}_f is unknown. Since the fluid particles in the LBM are always considered to move one cell length per time step, the fluid particles would come to rest at an intermediate node \mathbf{x}_i . In order to calculate the reflected distribution function in node \mathbf{x}_f , an interpolation scheme has to be applied [33].

Velocity and temperature in curved boundary condition

To calculate the distribution function in the solid region $\tilde{f}_{\bar{\alpha}}(\mathbf{x}_b, t)$ based upon the boundary nodes in the fluid region, the bounce back boundary conditions combined with interpolations including a one-half grid spacing correction at the boundaries [30, 33]. Then the Chapman-Enskog expansion for the post-collision distribution function on the eq. (17a) is conducted as:

$$\tilde{f}_{\bar{\alpha}}(\mathbf{x}_b, t + \Delta t) = (1 - \lambda)\tilde{f}_{\bar{\alpha}}(\mathbf{x}_f, t + \Delta t) + \lambda f_{\alpha}^*(\mathbf{x}_b, t + \Delta t) - 2\frac{3}{c^2} w_{\alpha} \rho(\mathbf{x}_f, t + \Delta t) \mathbf{e}_{\alpha} \mathbf{u}_w \quad (20)$$

where:

$$f_{\alpha}^*(\mathbf{x}_b, t + \Delta t) = f_{\alpha}^{\text{eq}}(\mathbf{x}_f, t + \Delta t) + \frac{3}{c^2} w_{\alpha} \rho(\mathbf{x}_f, t + \Delta t) \mathbf{e}_{\alpha} (\mathbf{u}_{\text{bf}} - \mathbf{u}_f) \quad (21)$$

$$\mathbf{u}_{\text{bf}} = \mathbf{u}_{\text{ff}}, \quad \lambda = \frac{2\Delta - 1}{\tau_m - 2}, \quad \text{if } 0 < \Delta \leq 0.5 \quad (22a)$$

$$\mathbf{u}_{\text{bf}} = \left(1 - \frac{3}{2\Delta}\right) \mathbf{u}_f + \frac{3}{2\Delta} \mathbf{u}_w, \quad \lambda = \frac{2\Delta - 1}{\tau_m + 0.5}, \quad \text{if } 0.5 < \Delta \leq 1 \quad (22b)$$

\mathbf{u}_{bf} and \mathbf{u}_w indicate imaginary velocity for interpolations and the velocity of wall. This study used the method is based on the reported method in [34] for temperature field in curved boundary. Distribution function for temperature divided two parts, equilibrium and non-equilibrium:

$$g_{\bar{\alpha}}(\mathbf{x}_b, t) = g_{\bar{\alpha}}^{\text{eq}}(\mathbf{x}_b, t) + g_{\bar{\alpha}}^{\text{neq}}(\mathbf{x}_b, t) \quad (23)$$

By substituting eq. (23) in eq. (17b) we have:

$$\tilde{g}_{\bar{\alpha}}(\mathbf{x}_b, t + \Delta t) = g_{\bar{\alpha}}^{\text{eq}}(\mathbf{x}_b, t) + \left(1 - \frac{1}{\tau_h}\right) g_{\bar{\alpha}}^{\text{neq}}(\mathbf{x}_b, t) \quad (24)$$

Obviously to calculate $\tilde{g}_{\bar{\alpha}}(\mathbf{x}_b, t + \Delta t)$, both $g_{\bar{\alpha}}^{\text{eq}}(\mathbf{x}_b, t)$ and $g_{\bar{\alpha}}^{\text{neq}}(\mathbf{x}_b, t)$ are required. Equilibrium and non equilibrium parts of eq. (24) are define as:

$$g_{\bar{\alpha}}^{\text{eq}}(\mathbf{x}_b, t) = w_{\bar{\alpha}} T^* \left(1 + \frac{3}{c^2} \mathbf{e}_{\bar{\alpha}} \mathbf{u}_b^*\right) \quad (25)$$

$$\begin{aligned} g_{\bar{\alpha}}^{\text{neq}}(\mathbf{x}_b, t) &= g_{\bar{\alpha}}^{\text{neq}}(\mathbf{x}_f, t) && \text{if } \Delta \geq 0.75 \\ g_{\bar{\alpha}}^{\text{neq}}(\mathbf{x}_b, t) &= \Delta g_{\bar{\alpha}}^{\text{neq}}(\mathbf{x}_f, t) + (1 - \Delta) g_{\bar{\alpha}}^{\text{neq}}(\mathbf{x}_{\text{ff}}, t) && \text{if } \Delta < 0.75 \end{aligned} \quad (26)$$

where

$$\begin{aligned} \mathbf{u}^* &= \frac{\mathbf{u}_w + (\Delta - 1)\mathbf{u}_f}{\Delta} && \text{if } \Delta \geq 0.75 \\ \mathbf{u}^* &= \frac{\mathbf{u}_w + (\Delta - 1)\mathbf{u}_f + (1 - \Delta)[2\mathbf{u}_w + (\Delta - 1)\mathbf{u}_{\text{ff}}]}{(1 + \Delta)} && \text{if } \Delta < 0.75 \end{aligned} \quad (27)$$

$$\begin{aligned} T^* &= \frac{(T_w + (\Delta - 1)T_f)}{\Delta} && \text{if } \Delta \geq 0.75 \\ T^* &= \frac{T_w + (\Delta - 1)T_f + (1 - \Delta)[2T_w + (\Delta - 1)T_{\text{ff}}]}{1 + \Delta} && \text{if } \Delta < 0.75 \end{aligned} \quad (28)$$

In order to calculate accurate forces on the moving walls, the momentum exchange method is used, which already showed good results in [33]. The momentum exchange method for the LBM is based upon the transfer of momentum by fluid particles to a particle surface after the streaming step.

The total force acting on a particle is then calculated as:

$$\mathbf{F} = \sum_{\text{all } x_b} \sum_{\alpha=1}^8 e_{\alpha} [f_{\alpha}(x_b, t) + f_{\bar{\alpha}}(x_b, t)] [1 - w(x_b)] \quad (29)$$

where, $w(x_f)$ is an indicator which is 0 and 1 when x_f location is occupied by fluid and solid, respectively.

Multi-relaxation-time model

The multi-relaxation-time lattice Boltzmann equation reads:

$$f_{\alpha}(\mathbf{x} + e_{\alpha} \Delta t, t + \Delta t) - f_{\alpha}(\mathbf{x}, t) = -[S_{\alpha i}] [f_i(\mathbf{x}, t) - f_i^{\text{eq}}(\mathbf{x}, t)] \quad (30)$$

The nine eigenvalues of matrix [S] are all between 0 and 2 so as to maintain linear stability and the separation of scales, which means that the relaxation times of non-conserved quantities are much faster than the hydrodynamic time scales. Equation (10) is the special case in which the nine relaxation times are all equal, and the collision matrix [S] = $1/\tau_m$ [I], where [I] is the identity matrix. Like eq. (17), eq. (30) includes two steps, collision and streaming:

$$\tilde{f}_{\alpha}(\mathbf{x}, t + \Delta t) - f_{\alpha}(\mathbf{x}, t) = -[S_{\alpha i}] [f_i(\mathbf{x}, t) - f_i^{\text{eq}}(\mathbf{x}, t)] \quad (31)$$

$$f_{\alpha}(\mathbf{x} + e_{\alpha} \Delta t, t + \Delta t) = \tilde{f}_{\alpha}(\mathbf{x}, t + \Delta t) \quad (32)$$

The collision step can be mapped to the momentum space by multiplying through by a transformation matrix [M] and the streaming is still finished in the velocity space. The multiple-relaxation-time lattice Boltzmann equation, eq. (30) becomes:

$$\mathbf{f}(\mathbf{x} + e_{\alpha} \Delta t, t + \Delta t) - \mathbf{f}(\mathbf{x}, t) = -[\mathbf{M}]^{-1} [\hat{\mathbf{S}}] [\hat{\mathbf{f}}(\mathbf{x}, t) - \hat{\mathbf{f}}^{\text{eq}}(\mathbf{x}, t)] \quad (32)$$

where $\mathbf{f} = [\mathbf{M}]\mathbf{f}$ and the bold-face symbols denote 9 dimensional column vectors, *e. g.* $\mathbf{f}(\mathbf{x}, t) = [f_0(\mathbf{x}, t), f_1(\mathbf{x}, t), \dots, f_8(\mathbf{x}, t)]$. The collision matrix [S] = $[\mathbf{M}\mathbf{S}\mathbf{M}]^{-1}$ in moment space is a diagonal matrix given by:

$$[\hat{\mathbf{S}}] = \text{diag}[0, s_2, s_3, 0, s_5, 0, s_7, s_8, s_9] \quad (33)$$

and \mathbf{f}^{eq} is the equilibrium value of the moment \mathbf{f} . The transformation matrix [M] can be constructed via the Gram-Schmidt orthogonalization procedure. Ginzburg [35] has been proposed the general form of the transformation matrix. Following the method by Ginzburg, the transformation matrix [M] of multi-relaxation-time model is obtained:

$$[M] = \begin{bmatrix} 1 & 1 & 1 & 1 & 1 & 1 & 1 & 1 & 1 \\ -4 & -1 & -1 & -1 & -1 & 2 & 2 & 2 & 2 \\ 4 & -2 & -2 & -2 & -2 & 1 & 1 & 1 & 1 \\ 0 & 1 & 0 & -1 & 0 & 1 & -1 & -1 & 1 \\ 0 & -2 & 0 & 2 & 0 & 1 & -1 & -1 & 1 \\ 0 & 0 & 1 & 0 & -1 & 1 & 1 & -1 & -1 \\ 0 & 0 & -2 & 0 & 2 & 1 & 1 & -1 & -1 \\ 0 & 1 & -1 & 1 & -1 & 0 & 0 & 0 & 0 \\ 0 & 0 & 0 & 0 & 0 & 1 & -1 & 1 & -1 \end{bmatrix} \quad (34)$$

The corresponding equilibrium distribution functions in moment space $\hat{\mathbf{f}}^{eq}$ are given by:

$$\mathbf{f}^{eq} = [\rho, e^{eq}, e^{2eq}, u_x, q_x^{eq}, u_y, q_y^{eq}, p_{xx}^{eq}, p_{xy}^{eq}]^T \quad (35)$$

where

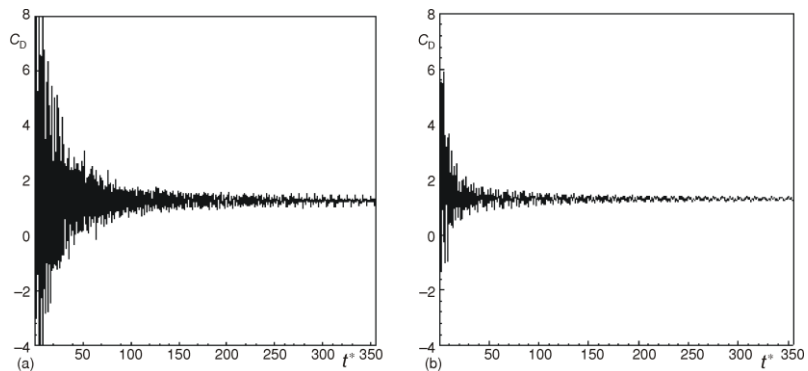
$$\begin{aligned} e^{eq} &= -2\rho + 3(u_x^2 + u_y^2), & e^{2eq} &= \rho - 3(u_x^2 + u_y^2), & q_x^{eq} &= -u_x, \\ q_y^{eq} &= -u_y, & p_{xx}^{eq} &= u_x^2 - u_y^2, & p_{xy}^{eq} &= u_x u_y \end{aligned} \quad (36)$$

In Lallemand *et al.* [36], it was shown that for the multi-relaxation-time (MRT) model to give the same shear viscosity as given by $\nu = c_s^2(\tau_m - 0.5)$ for the single-relaxation-time model, one can set:

$$s_8 = s_9 = \frac{1}{\tau_m} \quad (37)$$

It is necessary to choose the rest of the relaxation parameters, $s_2, s_3, s_5,$ and s_7 . In general, these four parameters can be chosen to be slightly larger than 1. Figure 4 shows the comparison of performance of MRT and single-relaxation time (SRT). This figure shows the time historic of drag coefficient for $Re = 50, K = 0.1,$ and $\beta = 1$. As it can be seen, the results of SRT consequently time is very noisy rather than MRT results, consequently time-average drag coefficient has accurate quantity.

Figure 4. Comparison of drag coefficient as a function of time between (a) SRT and (b) MRT, for $Re = 50, K = 0.1,$ $\beta = 1$



Verification and simulation

Figure 1 shows the computational domain of flow and heat transfer around a rotating isothermal circular cylinder of diameter D with uniform-shear flow in entrance and co-ordinates system. The initial values of velocity field are $u_x(x,y) = U_c$, $u_y(x,y) = 0$. The following dimensionless numbers are used to show the results:

$$t^* = \frac{2Ut}{D}, \quad x^* = \frac{2x}{D}, \quad y^* = \frac{2y}{D}, \quad u^* = \frac{u}{U_c}, \quad v^* = \frac{v}{U_c}, \quad T^* = \frac{T - T_\infty}{T_c - T_\infty} \quad (38)$$

To verify this study, flow around a rotating circular cylinder with constant velocity inlet and temperature is simulated. In a rectangular domain, the origin is located at the centre of the circular cylinder and the co-ordinates x and y are taken, respectively, to be measured along the horizontal and vertical directions. The upper and lower boundaries are set as free-slip velocity boundaries. At the inlet, fluid enters in x -direction in the domain with constant temperature and uniform velocity U_c and exits with fully developed profile.

The evolution of wake flow pattern around the cylinder at $Re = 200$, $\beta = 0.5$ for 3 different t^* is represented in fig. 5. Figures 5(a) and 5(b) show the streamlines obtained by present study and experimental results of Coutanceau *et al.* [6], respectively. The comparison between obtained results and experimental results shows good agreement in formation of wakes.

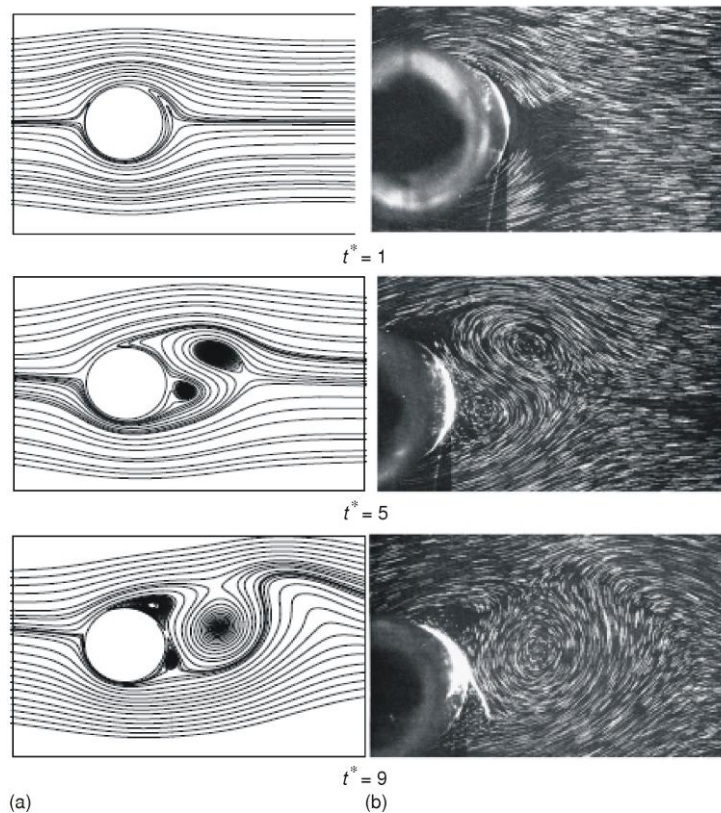


Figure 5. Comparison between the evolution of the velocity field for $Re = 200$, and $\beta = 0.5$ (a) obtained by present computation and (b) experiment [6]

Variations of u^* and v^* with time are compared with the experimental results of Coutanceau *et al.* [6] in fig. 6. These results are presented at $Re = 200$ and $\beta = 0.5$ at different t^* . The comparison indicates that the results have noticeable agreement with experimental data. Because of the lack of available experimental and numerical data for heat transfer, the results of present study are compared with those of numerical simulation of finite volume method (FVM) [37] and LBM [34] for the same problem at $Re = 200$, $\beta = 0.5$, and $Pr = 0.5$.

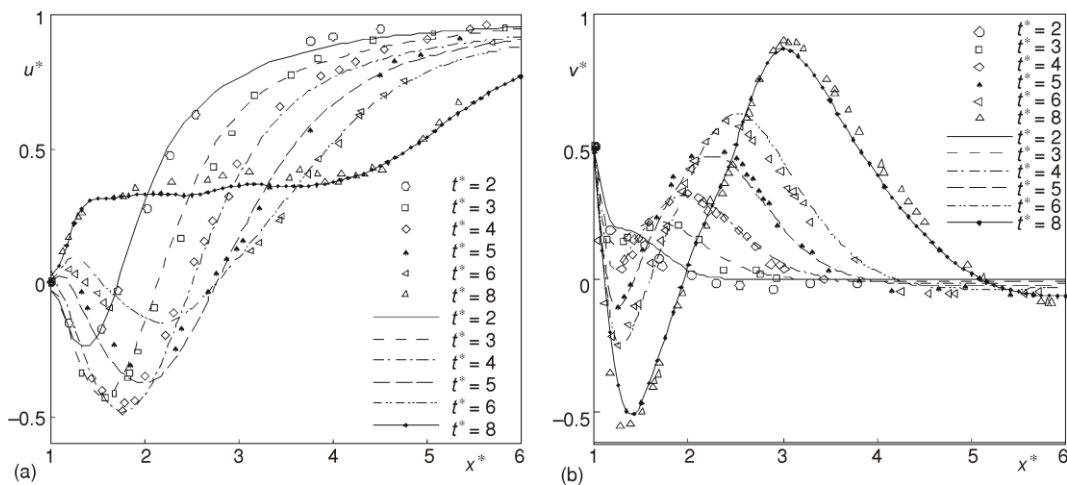


Figure 6. Time development of velocity profiles on x-axis for $Re = 200$ and $\beta = 0.5$; (a) u^* and (b) v^* obtained by experiments (symbols) [6] and present study (lines)

The comparison of temperature profiles obtained by present study and the FVM [37] is shown in fig. 7. Clearly, the two results are coherent however it is more difficult to handle this type of rotating boundary conditions in this FVM study. Figure 8 shows the growth of temperature contours with velocity streamlines at $Re = 200$, $\beta = 0.5$, and $Pr = 0.5$. The comparison between present study results and those obtained by Yan *et al.* [34] shows good agreement in formation of wakes.

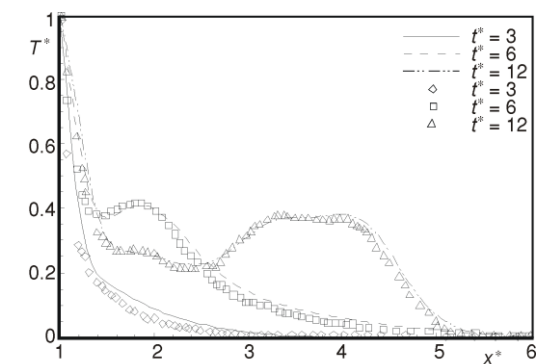


Figure 7. Comparison of temperature distributions on x-axis obtained by present study (symbols) and FVM (lines) [37] at $Re = 200$, $\beta = 0.5$, and $Pr = 0.5$

To check more accordance of heat transfer of the present study and experimental data, fig. 9 shows the distribution of period averaged Nusselt number on the surface of the cylinder. These results are compared with the results of Eckert *et al.* [38] that are calculated at $Re = 218$, $\beta = 0.0$, and $Pr = 0.71$.

These results are compared with the results of Eckert *et al.* [38] that are calculated at $Re = 218$, $\beta = 0.0$, and $Pr = 0.71$.

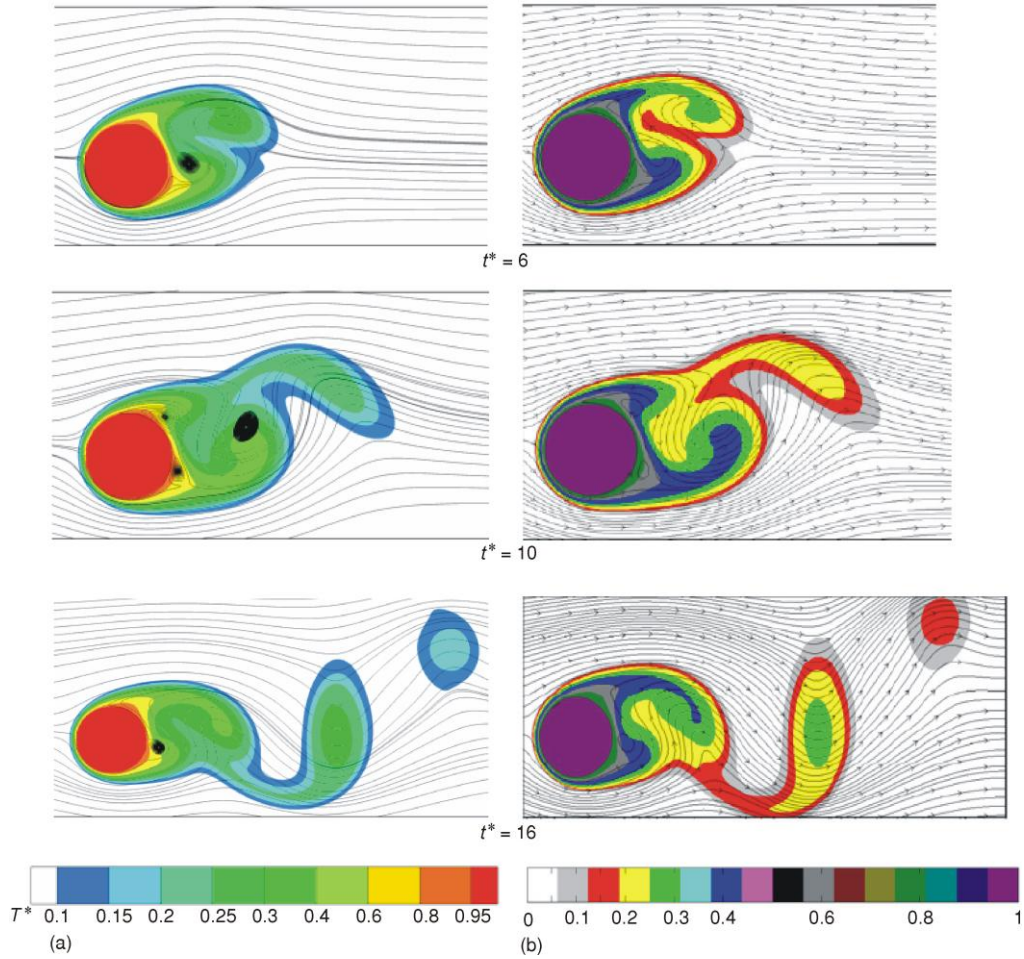


Figure 8. Comparison between the evolution of the temperature field for $Re = 200$, $\beta = 0.5$, and $Pr = 0.5$ obtained by (a) present study and (b) previous numerical study [34] (color image see on our web site)

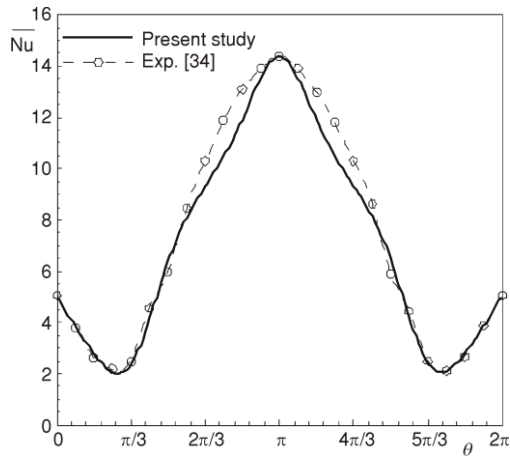


Figure 9. Distribution of period-averaged Nusselt number on the cylinder surface at $Re = 218$, $\beta = 0$, and $Pr = 0.71$

Results and discussion

After verifying the numerical method, we have conducted numerical simulations at various range of Reynolds number ($50 \leq Re \leq 160$), three rotational speed ratios of 0, 0.5, and 1 at shear rate $K = 0.1$, blockage ratio $B = 0.1$ and $Pr = 0.71$.

Isotherms and vorticity contours

Figure 10 shows the variations of the vortex-shedding frequency with the Reynolds number and rotational speed ratio in uniform-shear flow over a rotating circular cylinder. According to fig. 10(a), with increasing Reynolds number, the shedding frequency markedly increases all over the ranges of the rotational speed ratio considered in the present study. Such correlation between the shedding frequency and Reynolds number agrees well with those of Kang [39]. On the other hand, the shedding frequency slightly increases with increasing rotational speed ratio. In the laminar regime, the effect of Reynolds number on the vortex-shedding frequency is overall very strong compared with those of other parameters. To more closely reveal the rotating effect, the variation of the shedding frequency with the rotational speed ratio is presented in fig. 10(b) for the uniform-shear flow at difference Reynolds

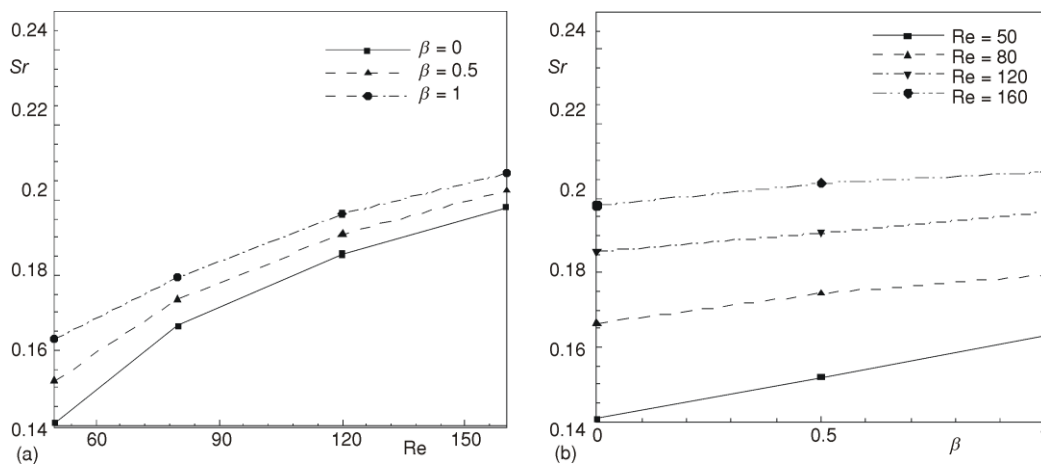


Figure 10. Vortex-shedding frequencies (Sr) with respect to (a) Re and (b) β

numbers. The effect of Re number on instantaneous vorticity contours (ω_z) and isotherms are shown in fig. 11. As it can be seen in fig. 11, vortex formation for different Re and at a specific time is shown. At $Re = 50$ vortex core stretches and does not allow the vortex to shed. Increasing the Re number decrease the length of vortex core, hence the shedding frequency increases. As both vorticity and thermal energy are transported by the flow, the vorticity contours and the isotherms exhibit similar features. Figure 12 shows the effect of rotational speed ratio (β) on flow and heat transfer fields. Vorticity contours at left and the isotherms at right for $Re = 160$, $Pr = 0.72$, and shear rate $K = 0.1$ are shown in fig. 12. The cylinder does not rotate when $\beta = 0$, the vortices are asymmetric and shed alternatively downstream and meanwhile the heat advects to the downstream similar to the vortices, fig. 12(a). When $\beta \neq 0$, differences in the vorticity and isotherm contours become obvious. Because the upper side of the cylinder moves against the stream whereas the lower one moves

in the direction of stream the wall shear gradient is asymmetrical. Evidently, the periodic vortex shedding still remains. Besides advection of vorticity, also heat is advected into the cylinder wake as can be seen in fig. 12.

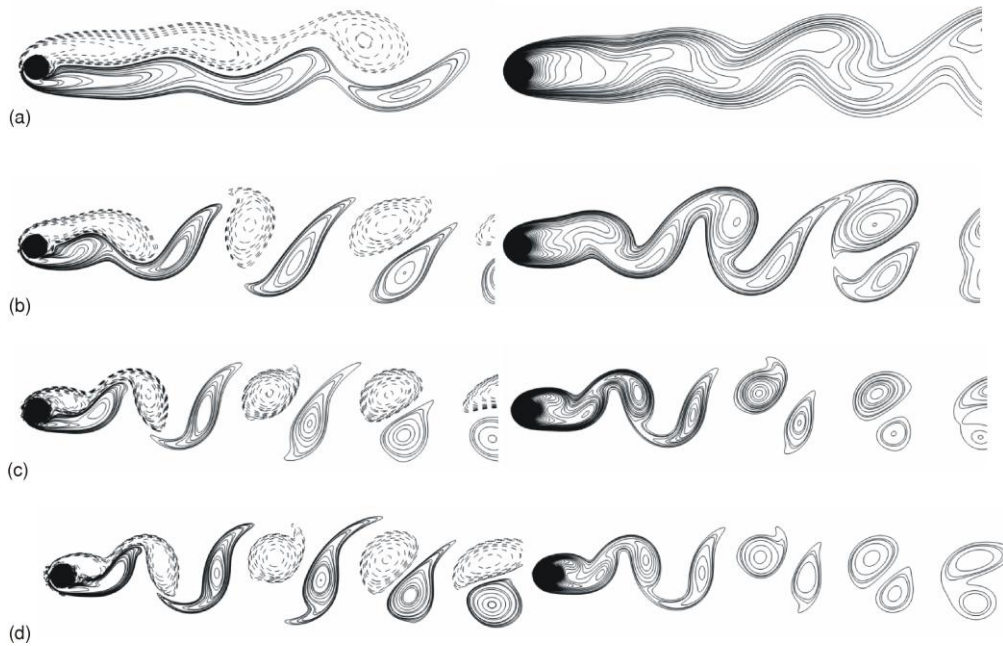


Figure 11. Vorticity (on the left) and isotherms (on the right) contours for $Pr = 0.71$ and $\beta = 0.5$ at $t^* = 355$; (a) $Re = 50$, (b) $Re = 80$, (c) $Re = 120$, and (d) $Re = 160$

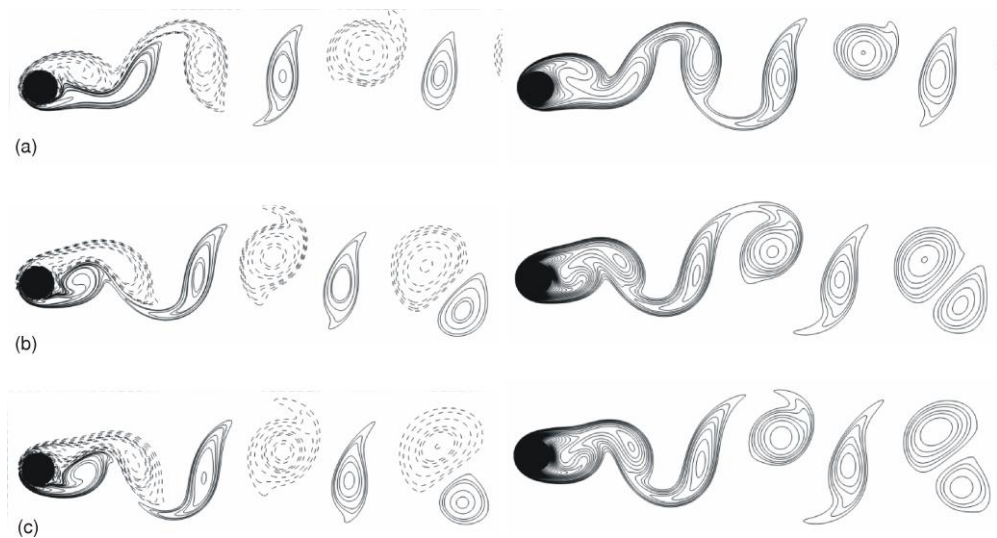


Figure 12. Vorticity (on the left) and isotherms (on the right) contours for $Pr = 0.71$ and $Re = 160$ at $t^* = 660$; (a) $b = 0$, (b) $b = 0.5$, and (c) $b = 1$

The heat is advected from cylinder wall in the near wake in a way similar to the advection of vorticity. The similarity between advection of vorticity and heat implies that the vortex structures are hot isolated areas with a strong circulation. However, one of the differences which can be observed is the size of the hot core and the vortex structure. As can be seen, the hot core is more compact than the vortex structure. Due to the fact that heat is captured in the kernel of the vortex structure, only diffusion process can cause the hot core to spread.

Force acting on cylinder

To examine the Re number and rotational speed ratio (β) effects on the force acting, the time average and time historic values of drag and lift coefficients are shown in figs. 13, 14, and 15. Obviously fig. 13 shows that \overline{C}_D and \overline{C}_L values do not change significantly at different Re numbers. The maximum variation is 6.5% and 7% for \overline{C}_D and \overline{C}_L respectively.

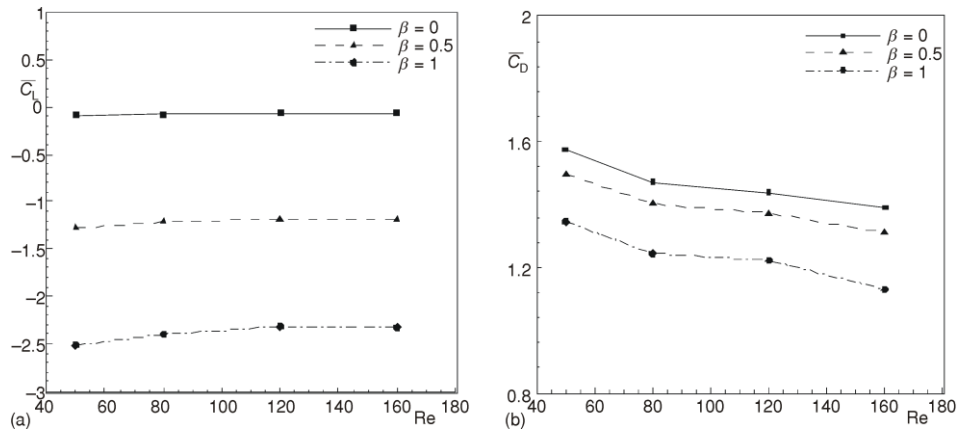


Figure 13. Time-averaged lift and drag coefficients as a function of Reynolds number for different rotational speed ratios: (a) \overline{C}_L and (b) \overline{C}_D

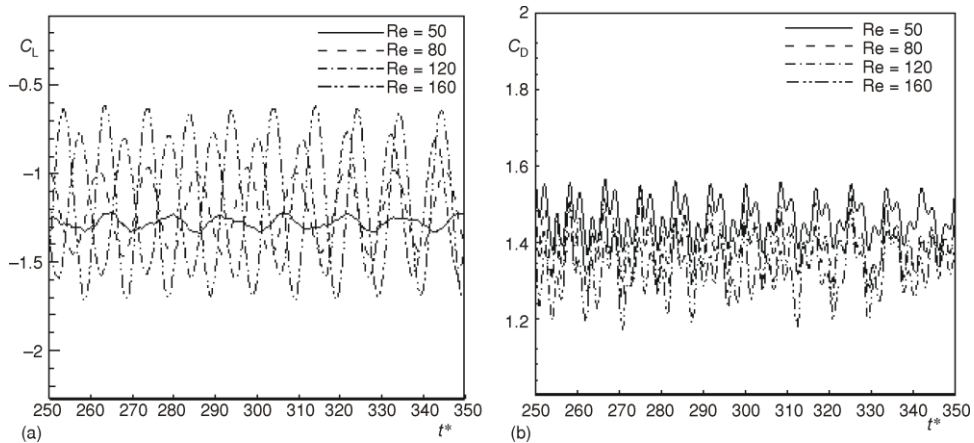


Figure 14. Time-historic lift and drag coefficients at different Reynolds numbers for $\beta = 0.5$; (a) C_L and (b) C_D

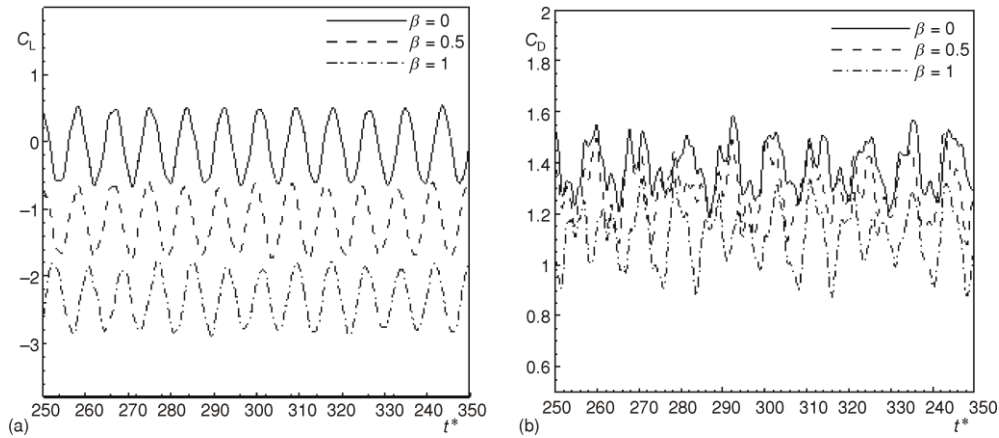


Figure 15. Time-historic lift and drag coefficients for different rotational speed ratios at $Re = 160$; (a) C_L and (b) C_D

It should be mentioned that, because of the counterclockwise rotation of the cylinder, the time averaged lift coefficient, $\overline{C_L}$ for all β are less than zero. The negative value for $\overline{C_L}$ at $\beta = 0$ is due to the shear effect that results the pressure over the top part of cylinder becomes higher than that under the bottom part. As it can be seen in fig. 13(b), when β increases from 0 to 1 $\overline{C_D}$ decreases. It's due to the significantly reduce of wake length behind the cylinder as a result of the cylinder rotation. It should be mentioned that the rotation of cylinder accelerates the detachment of vortices. Figure 14 shows time historic values of drag and lift coefficients for $Re = 160$ and different β . As can be seen, for lift coefficient the amplitude of the oscillation increases while the mean values do not change noticeably, and for drag coefficient the changes of amplitude of the oscillation and mean values are negligible. In contrary, the rotational speed ratio changes the mean value of the lift coefficient meanwhile the amplitude of oscillation does not change significantly as shown in fig.15.

Nusselt number variations

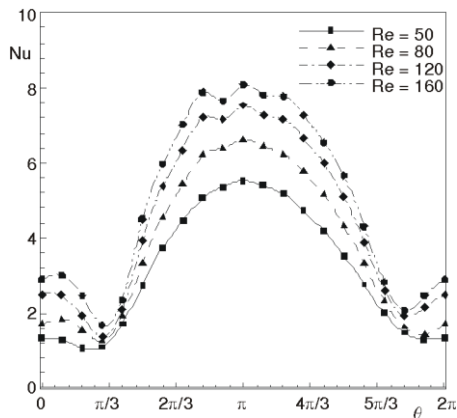


Figure 16. Local Nusselt number at $t^* = 355$ for $\beta = 0.5$ and different Reynolds numbers

The variation of local Nusselt number for different Re at $t^* = 355$ are shown in fig. 16. It can be seen from the figure that, for all four different Re numbers, there are two local minimum and one maximum. Due to the smaller thermal resistance, the local Nu at the forward stagnation point is highest and decreases up to the point of separation. In the wake region, where the vortices are formed and shed, a further increase in Nu number can be seen because of good mixing. Due to the influence of vortex shedding, the local Nu number distribution in the wake region varies temporally. However, these variations are averaged out for the purpose of comparison. Figure 17 depicts the

periodic average Nu number variation with rotational speed ratio at $Re = 50$ and 160 . It is expected that the peak of the Nu distribution shifts to the right, due to the rotation of cylinder, but the maximum value stays at $\theta = \pi$ as a result of the shear effect. The rotation of the cylinder pushes forward the point of flow separation, hence, the minimum point of Nu distribution on the cylinder surface shift to the right.

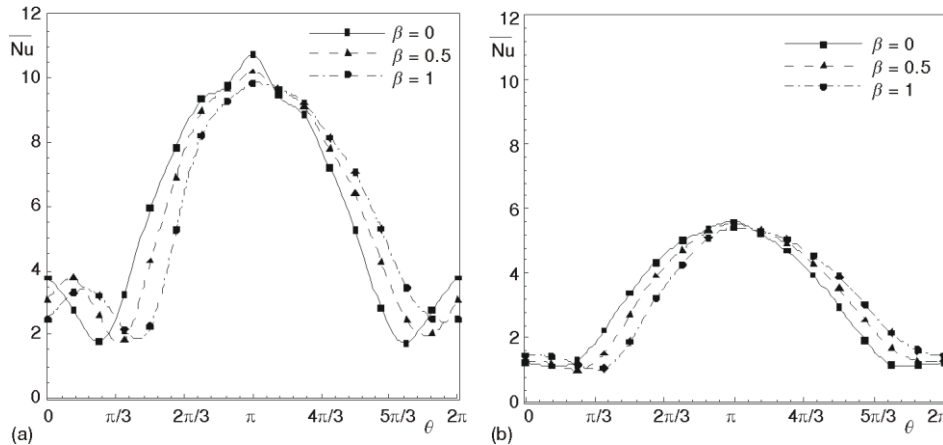


Figure 17. Periodic averaged Nusselt number for different rotational speed ratios β ; (a) $Re = 160$ and (b) $Re = 50$

For better discussion present investigation is concluded by exploring the effect of Re number and rotational speed ratio on the period-surface average Nu number outcome as indicated in fig. 18. As it mentioned before the effect of Reynolds number on the vortex-shedding frequency is overall very strong in compare with rotational speed ratio. It is concluded that the Re number increment, increases the period-surface average Nu number due to the good mixing of the vortices and the high shed frequency. Although the increase of the rotational speed ratio increases the Nu, but it is slight in compare with Re number.

Conclusions

The present study has applied lattice Boltzmann method to simulate numerically two-dimensional laminar flow and heat transfer over a rotating circular cylinder with a uniform planar shear, where the free-stream velocity varies linearly across the cylinder using MRT method. The range of Reynolds numbers $50 \leq Re \leq 160$ for three rotational speed ratios of 0, 0.5, and 1, and $K = 0.1$ are investigated. The results show that in the laminar regime, the effect of Reynolds number on the vortex-shedding frequency is overall very strong compared

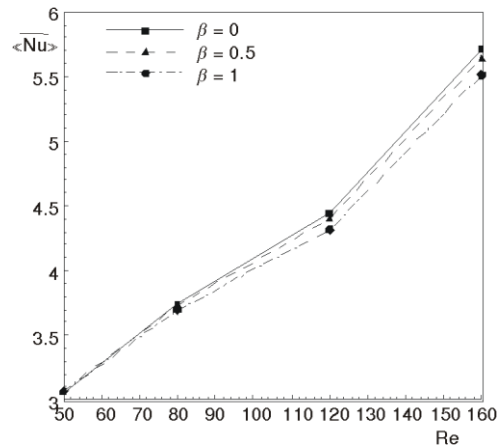


Figure 18. Periodic and surface averaged Nusselt number at different rotational speed ratios β and Reynolds numbers

with rotational speed ratio. The results of SRT are very noisy rather than MRT results; consequently accuracy of MRT model is more than SRT model. In addition variation of $\overline{C_D}$ and $\overline{C_L}$ values strongly depends on rotational speed ratio (β) and do not change significantly with Reynolds number. In heat transfer field it is expected that the peak of the Nu distribution shifts to the right, due to the rotation of cylinder, but the maximum value stays at $\theta = \pi$ as a result of the shear effect. The rotation of the cylinder pushes forward the point of flow separation, hence, the minimum point of Nu distribution on the cylinder surface shift to the right.

Nomenclature

B	– non-dimensional parameter – blockage ratio $[D/W]$, [–]	Pr	– Prandtl number ($= \nu/\alpha$), [–]
C_D	– drag coefficient $[(= 2F_x/(\rho U_c D))]$, [–]	Re	– Reynolds number ($= U_c D/\nu$), [–]
C_L	– lift coefficient $[(= 2F_y/(\rho U_c D))]$, [–]	T	– temperature, [K]
c_s	– speed of sound in lattice scale, [–]	t	– time, [s]
\overline{D}	– diameter of cylinder, [m]	T_h	– hot temperature, [K]
e_i	– discrete lattice velocity in direction i , [–]	T_c	– cold temperature, [K]
F	– force, [N]	U_c	– stream wise velocity at the center-line, $[\text{ms}^{-1}]$
F_x	– force in x-direction, [N]	U	– inlet velocity profile ($= U_c + Gy$), $[\text{ms}^{-1}]$
F_y	– force in y-direction, [N]	u, v	– horizontal and vertical components of the velocity, $[\text{ms}^{-1}]$
f_i	– velocity distribution function (pre-collision), [–]	W	– lateral width, [m]
\tilde{f}_i	– velocity distribution function (post-collision), [–]	w_k	– weighting factor, [–]
f_i^{eq}	– equilibrium distribution function of velocity, [–]	x	– horizontal direction, [m]
G	– lateral velocity gradient ($= dU/dy$), $[\text{s}^{-1}]$	y	– vertical direction, [m]
g_i	– temperature distribution function (pre-collision), [–]	Greek symbols	
\tilde{g}_i	– temperature distribution function (post-collision), [–]	β	– rotational speed ratio ($= D\omega/2U_c$), [–]
g_i^{eq}	– equilibrium distribution function of temperature, [–]	ν	– kinematic viscosity, $[\text{m}^2\text{s}^{-1}]$
g_y	– acceleration due to gravity, $[\text{ms}^{-2}]$	ρ	– density, $[\text{kgm}^{-3}]$
K	– non-dimensional velocity gradient or shear rate ($= DG/U_c$), [–]	τ_m	– lattice relaxation time for f , [–]
Nu	– local Nusselt number	τ_h	– lattice relaxation time for g , [–]
$\langle \overline{\text{Nu}} \rangle$	$[(= D(\partial T/\partial n)_{\text{cylinders surface}}/(T_h - T_\infty))]$, [–]	ω	– angular velocity of the cylinder, $[\text{s}^{-1}]$
	$[\int_{t_p} 1/t_p \int_p \langle \text{Nu} \rangle dt]$, [–]	Subscripts	
		c	– cold
		h	– hot
		i	– spatial indices

References

- [1] Bearman, P. W., Wadcock, A. J., The Interaction between a Pair of Circular Cylinder Normal to a Stream, *J. Fluid Mech.*, 61 (1973), 3, pp. 499-511
- [2] Triyogi, Y., Suprayogi, D., Spirda, E., Reducing the Drag on a Circular Cylinder by Upstream Installation of an I-Type Bluff Body as Passive Control, *Proc. IMechE, Part C: J. Mechanical Engineering Science*, 223 (2009), 10, pp. 2291-2296
- [3] Nair, M. T., Sengupta, T. K., Chauhan, U. S., Flow Past Rotating Cylinders at High Reynolds Numbers Using Higher Order Upwind Scheme, *Comput. Fluids*, 27 (1998), 1, pp. 47-70
- [4] Marchesse, Y., Changenet, C., Forced Convective Heat Transfer over a Non-Circular Slender Cylinder, *Proc. IMechE, Part C: J. Mechanical Engineering Science*, 223 (2009), 2, pp. 427-437

- [5] Kim, H. J., Durbin, P. A., Investigation of the Flow between a Pair of Circular Cylinders in the Flopping Regime, *J. Fluid Mech.*, 196 (1988), pp. 431-48
- [6] Coutanceau, M., Menard, C., Influence of Rotation on the Near-Wake Development behind an Impulsively Started Circular Cylinder, *J. Fluid Mech.*, 158 (1985), pp. 399-466
- [7] Sumner, D., *et al.*, Fluid Behavior of Side-by-Side Circular Cylinders in Steady Cross-Flow, *J. Fluids Struct.*, 13 (1999), 3, pp. 309-338
- [8] Adachi, T., Kato, E., Study on the Flow about a Circular Cylinder in Shear Flow, *Trans. Jpn. Soc. Aeronaut. Space.*, 256 (1975), pp. 45-53
- [9] Kiya, M., Tamura, H., Arie, M., Vortex Shedding from a Circular Cylinder in Moderate-Reynolds-Number Shear Flow, *J. Fluid Mech.*, 141 (1980), 4, pp. 721-735
- [10] Hayashi, T., Yoshino, F., On the Evaluation of the Aerodynamic Forces Acting on a Circular Cylinder in a Uniform Shear Flow, *Trans. Jpn. Soc. Mech. Eng.*, 56 (1990), 552, pp. 31-36
- [11] Kwon, T. S., Sung, H. J., Hyun, J. M., Experimental Investigation of Uniform Shear Flow Past a Circular Cylinder, *ASME J. Fluids Eng.*, 114 (1992), 3, pp. 457-460
- [12] Sumner, D., Akosile, O. O., On Uniform Planar Shear Flow around a Circular Cylinder at Subcritical Reynolds Number, *J. Fluids Struct.*, 13 (2003), 3-4, pp. 309-338
- [13] Tamura, H., Kiya, M., Arie, M., Numerical Simulation of the Shear Flow Past a Circular Cylinder, *Trans. Jpn. Soc. Mech. Eng.*, 46 (1980), 404, pp. 555-564
- [14] Lei, C., Cheng, L., Kavanagh, K., A Finite Difference Solution of the Shear Flow over a Circular Cylinder, *Ocean Eng.*, 27 (2000), 3, pp. 271-290
- [15] Sohankar, A., Norberg, C., Davidson, L., Simulation of Three-Dimensional Flow around a Square Cylinder at Moderate Reynolds Number, *Phys. Fluids*, 11 (1999), 2, pp. 288-306
- [16] Jordan, S. K., Fromm, J. E., Laminar Flow Past a Circle in a Shear Flow, *Phys. Fluids*, 15 (1972), 6, pp. 972-976
- [17] Delavar, M. A., Farhadi, M., Sedighi, K., Effect of the Heater Location on Heat Transfer and Entropy Generation in the Cavity Using the Lattice Boltzmann Method, *Heat Trans Res.*, 40 (2009), 6, pp. 505-519
- [18] Djebali, R., Ganaoui, M. E., Sammouda, H., Bennacer, R., Some Benchmarks of a Side Wall Heated Cavity using Lattice Boltzmann Approach, *FDMP*, 5 (2009), 3, pp. 261-282
- [19] Ganaoui, M. E., Semma, E. A., A Lattice Boltzmann Coupled to Finite Volumes Method for Solving Phase Change Problems, *Thermal Science*, 13 (2009), 2, pp. 205-216
- [20] Semma, E. A., *et al.*, Investigation of Flows in Solidification by Using the Lattice Boltzmann Method, *Int. J. of Thermal Sciences*, 47 (2008), 3, pp. 201-208
- [21] Semma, E. A., Ganaoui, M. E., Bennacer, R., Lattice Boltzmann Method for Melting/Solidification Problems, *Comptes Rendus Mécanique*, 335 (2007), 5-6, pp. 295-303
- [22] Nemati, H., *et al.*, Numerical Simulation of Fluid Flow around Two Rotating Side by Side Circular Cylinders by Lattice Boltzmann Method, *International Journal of Computational Fluid Dynamics*, 24 (2010), 3, pp. 83-94
- [23] Moussaoui, M. A., *et al.*, MRT-Lattice Boltzmann Simulation of Forced Convection in a Plane Channel with an Inclined Square Cylinder Original Research Article, *Int. J. of Thermal Sciences*, 49 (2010), 1, pp. 131-142
- [24] Breyiannis, G., Valougeorgis, D., Lattice Kinetic Simulations of 3-D MHD Turbulence, *Comput. Fluids*, 35 (2006), 8-9, pp. 920-924
- [25] Lee, K., Yu, D., Girimaji, S. S., Lattice Boltzmann DNS of Decaying Compressible Isotropic Turbulence with Temperature Fluctuations, *Int. J. Comput. Fluid Dyn.*, 20 (2006), 6, pp. 401-413
- [26] Yoshino, M., Matsuda, Y., Shao, C., Comparison of Accuracy and Efficiency between the Lattice Boltzmann Method and the Finite Difference Method in Viscous/Thermal Fluid Flows, *Int. J. Comput. Fluid Dyn.*, 18 (2004), 4, pp. 333-345
- [27] Huang, H., *et al.*, Shan-and-Chen-Type Multiphase Lattice Boltzmann Study of Viscous Coupling Effects for Two-Phase Flow in Porous Media, *Int. J. Numer. Meth. Fluids*, 61 (2009), 3, pp. 341-354
- [28] Aminfar, H., Mohammadpourfard, M., Lattice Boltzmann BGK Model for Gas Flow in a Microchannel, *Proc. IMechE, Part C: J. Mechanical Engineering Science*, 222 (2008), 9, pp. 1855-1860
- [29] Wolf-Gladrow, D. A., Lattice-Gas Cellular Automata and Lattice Boltzmann Models, Springer, 2000
- [30] Yu, D., *et al.*, Viscous Flow Computations with the Method of Lattice Boltzmann Equation, *Prog. Aerosp. Sci.*, 39 (2003), 5, pp. 329-367
- [31] Guo, Z., Shi, B., Zheng, C., A Coupled Lattice BGK Model for the Boussinesq Equations, *Int. J. Numer. Methods Fluids*, 39 (2002), 4, pp. 325-342

- [32] Barrios, G., *et al.*, The Lattice Boltzmann Equation for Natural Convection in a Two-Dimensional Cavity with a Partially Heated Wall, *J. Fluid Mech.*, 522 (2005), pp. 91-100
- [33] Mei, R., *et al.*, Force Evaluation in the Lattice Boltzmann Method Involving Curved Geometry, *Phys. Rev. E.*, 65 (2002), 4, pp. 1/041203-14/041203
- [34] Yan, Y. Y., Zu, Y. Q. Numerical Simulation of Heat Transfer and Fluid Flow Past a Rotating Isothermal Cylinder – A LBM Approach, *Int. J. of Heat Mass Transfer*, 51 (2008), 9-10, pp. 2519-2536
- [35] Ginzburg, I. Equilibrium-Type and Link-Type Lattice Boltzmann Models for Generic Advection and Anisotropic-Dispersion Equation, *Adv. Wat. Resour.*, 28 (2005), 11, pp. 1171-1195
- [36] Lallemand, P., Luo, L. S., Theory of the Lattice Boltzmann Method: Dispersion, Dissipation, Isotropy, Galilean Invariance, and Stability, *Phys Rev E*, 61 (2000), 6, pp. 6546-6562
- [37] Lai, H., Yan, Y. Y. The Effect of Choosing Dependent Variables and Cell-Face Velocities on Convergence of the SIMPLE Algorithm Using Non-Orthogonal Grids, *Int. J. Numer. Methods Heat Fluid Flow*, 11 (2001), 5/6, pp. 524-546
- [38] Eckert, E. R. G., Soehngen, E. Distribution of Heat Transfer Coefficients around Circular Cylinders in Cross-Flow at Reynolds Numbers from 20 to 500, *Trans. ASME*, 74 (1952), 3, pp. 343-347
- [39] Kang, S., Uniform-Shear Flow over a Circular Cylinder at Low Reynolds Numbers, *J. Fluids Struct.*, 22 (2006), 4, pp. 541-555